Ballistic impact studies of a borosilicate glass

L.C. Forde, W.G. Proud, S.M. Walley, P.D. Church, I.G. Cullis

Accepted Manuscript

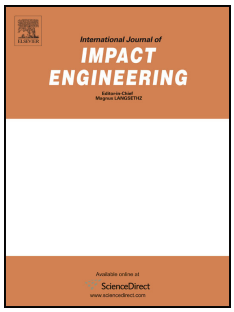

Title: Ballistic impact studies of a borosilicate glass

Authors: L.C. Forde, W.G. Proud, S.M. Walley, P.D. Church, I.G. Cullis

PII: S0734-743X(09)00186-9

DOI: 10.1016/j.ijimpeng.2009.10.005

Reference: IE 1843

To appear in: *International Journal of Impact Engineering*

Received Date: 18 February 2009

Revised Date: 7October2009

Accepted Date: 19 October 2009

Please cite this article as: Forde LC, Proud WG, Walley SM, Church PD, Cullis IG. Ballistic impact studies of a borosilicate glass, International Journal of Impact Engineering (2009), doi: 10.1016/ j.ijimpeng.2009.10.005

BALLISTIC IMPACT STUDIES OF A BOROSILICATE GLASS

L.C. Forde*, W.G. Proud, S.M. Walley†

Fracture and Shock Physics Group, Cavendish Laboratory, J.J. Thomson Avenue, Cambridge CB3 0HE, United Kingdom

P.D. Church, I.G. Cullis

QinetiQ Fort Halstead, Sevenoaks, Kent, TN14 7BP, United Kingdom

Abstract

The ballistic impact properties of a borosilicate ('pyrex') glass was studied using mild steel rods accelerated using a light gas gun. High-speed photography at sub-microsecond framing rates was used along with schlieren optics to investigate the propagation of elastic shock waves and fracture fronts. Flash X-radiography was used to visualize the deformation of rods as they penetrated the comminuted glass normally. The rod was seen initially to dwell on the surface for at least 3μs creating a Hertzian cone-crack. Later on, between 40 and 60 μs, self-sharpening of the projectile was observed as the 'wings' of the heavily deformed front end sheared off. After this event, the front of the rod speeded up. X-rays also showed that the pattern of fissures within the comminuted glass was observed to be very similar shot-to-shot. X-radiography was also used to examine the mechanisms occurring during oblique impact of rods at 45˚. In oblique impact, bending of the rod rather than plastic deformation ('mushrooming') takes on the role of distributing the load over an area larger than that of the original rod diameter. High-speed photography of the rear surface of a glass block on which a fine grid had been placed confirmed that the comminuted glass moved as larger interlocked blocks. The experiments were modelled using the QinetiQ Eulerian hydrocode GRIM making use of the Goldthorpe fracture model. The model was found to predict well the transition from dwell to penetration.

1. Introduction

The study of the ballistic impact of transparent materials allows the mechanisms of penetration and failure to be observed relatively easily. For example, failure of such materials may often be seen directly using high-speed photography. In addition, if a metal

* Now at the Measurement Standards Laboratory, New Zealand. † Corresponding author

projectile is used, the difference in free electron densities between target and penetrator can allow sufficient contrast for observation using flash X-rays.

By comparison with metals, silica-based glasses have high compressive yield strengths but low fracture toughness. Because of their excellent rigidity and strength per unit weight, they have been used in applications such as security glazing in vehicles and blast-proof windows in buildings [1-4].

The material chosen for study was the widely-used borosilicate glass, known also as 'pyrex', which has a dynamic yield strength of over 5 GPa and an open structure which allows a degree of compaction under shock [5-7].

2. Experimental

2.1 Apparatus

All the experiments reported in this paper were performed using a 50mm light gas gun [8]. As the rods were 9.5mm diameter and 95mm long, they were accelerated down the barrel using a polycarbonate sabot.

2.2 Schlieren optic studies

All the high-speed photographic sequences presented in this paper were taken using an FS501 Ultranac camera using back illumination by a flash tube. High-speed photography of intense stress waves in transparent media is often enhanced by the use of schlieren optics because discontinuities or sharp gradients in density and/or pressure may be visualised as bright and dark features.

Figure 1 presents selected frames from a high-speed photographic sequence of an impact between a 10mm hemispherical-nosed mild steel rod and a borosilicate target at 531 m s^{-1}. Relevant mechanical properties of the steel and the glass are given in Table 1. The nose of the rod is situated just outside the field of view, impinging upon the left edge of the frames. The rod impacted slightly above the marker line, which is drawn using a permanent marker pen on the side of the block along with ticks 5mm apart, the leftmost tick being 5mm from the impact surface. The glass blocks were 75mm square and 25mm thick. The frames are labelled with the time elapsed after the first frame, which was itself taken no more than 100ns after impact.

Figure 1. Near here

Table 1 near here

The initial elastic shock wave, curved due to the highly-localised initial loading of the glass can be seen as a bright wave-front moving away from the impact site towards the right. The wave speed measured from this sequence was 5.7±0.1 mm μs^{-1} which is in fairly good agreement with values in the literature, for example 5.97 mm μs^{-1} [9] and 6.05 mm μs^{-1} [10]. Caution must, however, be taken when interpreting measurements of wave velocity from such sequences for three reasons: (i) the hemispherical wave is expanding in three dimensions, including towards the camera; (ii) the axis of impact is within the target some 32mm distant from the marker on the surface, leading to magnification differences; (iii) there will be some refraction at the surface of the glass block for an off-axis optical path. Despite this, at 4.8μs the bright wave-front reappears, which is consistent with the known specimen thickness and measured wave velocity as being the tensile release wave reflected from the rear surface. However, the divergent nature of the wave means that we cannot infer that the glass is under compression for all of the intervening time. Indeed radial tensions could develop as the wave front expands.
Moving more slowly than the bright elastic stress wave is an opaque (black) front propagating at a steady velocity of 2.00±0.03 mm μs^{-1}. Once again caution must be exercised with this value. However, it falls within the range of single-crack propagation speeds of approximately 1.6 mm μs^{-1} for sodalime glass and 2.2 mm μs^{-1} for fused silica [9, 11]. The opacity is most likely due to cracks opening up to a width commensurate with the wavelength of light and thus scattering light from the flash away from the camera. The flat portion of the fracture front expands laterally as it travels through the glass eclipsing the curved edges and leaving a planar wave in the field of view by about 5μs.
The sequence from a similar experiment performed at 536 m s^{-1} is presented in figure 2. A hemispherical damage front can be seen propagating away from the impact site at 1.80±0.04 mm μs^{-1}. This sequence clearly demonstrates the transition of the fracture front from hemispherical to plane wave, beginning near the central axis. Two dark arcs appear in the first frame (labelled 0μs) at the 5mm marker resembling the double shock wave structure observed by Bourne and co-workers [12, 13] in plate impact experiments on pyrex as well as the transient double arcs seen during the loading cycle in impacts between steel

spheres and glass performed by Chaudhri and Kurkjian [14]. Using stress gauges, Bourne and co-workers measured two phases in the rise of stress from zero to the maximum value during shock loading: a first slower ramping stage implying compaction of the glass structure and then a steeper rise up to the final shock. This behaviour leads to two distinct phases of rapid stress change and thus probably explains the dual wave structure seen using schlieren optics in the experiment reported here. The black arcs seen in figure 2 fade away within about 1μs, presumably because the wave diverges and loses intensity quickly. It is also overtaken rapidly by the fracture front. It is not known why the elastic shock waves appear so different in the two experiments presented, except that schlieren systems are very sensitive to the precise way they are assembled.

Figure 2. Near here

Bourne and co-workers [10, 12, 13] saw similar opaque fracture fronts during plate impact experiments on borosilicate glass. These fronts followed a small distance behind the opaque band associated with the shock wave. They also had a rougher appearance than those produced in these rod impact experiments, but were nevertheless more uniform than fracture fronts seen in sodalime glass. However, when comparing plate and rod impact experiments we should note that in plate impact the material remains under compression during failure, whereas a rod produces divergent waves enabling tensile crack propagation. The phenomenon of failure under planar shock takes place under compression and shear. The velocity of propagation has been found to depend upon the velocity of the flyer plate, eventually merging with the shock wave for high enough values. The failure wave velocity measured by Bourne *et al.* for an impact velocity 250 m s^{-1} on pyrex was 3.4 mm μs^{-1}, greater than the maximum crack propagation predicted on the basis of the Rayleigh wave speed and significantly higher than the velocities measured in this study. For the case of a failure front propagating in a glass rod, Radford and co-workers found that for sufficiently high impact stresses the failure front propagated at a limiting velocity of $\sqrt{2}c_s$ [15] consistent with a suggestion by Rosakis and co-workers[16] that a single shear crack in an infinite medium could propagate at this velocity. However, in a later paper Willmott & Radford[17] found matters were more complex than this in that the velocity of failure fronts in glass rods above impact pressures of about 2 GPa were

scattered within a band between c_s and c_L. In conclusion, the failure front observed here probably has little in common with that observed in plate or rod impact experiments on the same material because both the magnitude and the nature of the stress fields are different in all three cases.

Instead, studies of the interaction of spherical impactors and indenters with glasses shed more light on the nature of the flattening behaviour of the failure front [9, 11, 14, 18, 19]. One phenomenon which is commonly seen is the Hertzian cone crack [18, 20, 21]. Hertz [22-24] first analysed the elastic stresses involved and found that the tensile stress has a maximum at the edge of the contact area and falls off with increasing radial distance. The tensile radial stress leads to a ring crack initiating at a defect usually just outside the actual contact area. The reason the ring crack forms at a larger radius is at least partly because of the interfacial shear stresses arising from the difference in elastic properties between the indenter and indented material. If loading is sustained, the ring crack develops into a cone which propagates into the solid [25].

Although the Hertzian analysis is for the static case, it has been extended to include impact [20]. Field and co-workers [26, 27] showed that a single cone can be recovered from soda-lime glasses at velocities up to *ca.* 40 m s^{-1} and from aluminas at velocities up to *ca.* 900 m s^{-1}. Above these velocities multiple cones form and fragment. In glasses, stress wave-induced fracture occurs at velocities above *ca.* 200 m s^{-1}.

The results reported here are consistent with those observations since the flattened part of the fracture front is indicative of cone crack formation and the damage outside this region is attributable to Rayleigh surface wave cracking. The region immediately under the impact is initially subjected to compression and shear, but not tension. At very high impact velocities failure may occur due to shear as in plate impact experiments. Tensile stresses will only form in this region as release waves arrive from free surfaces or other boundaries. This may happen before waves reflect from the rear surface since elastic waves will be emitted from fracture tips and can be trapped between the cone surfaces. Eventually we would expect the glass to be heavily fragmented (comminuted). However, this fragmented material will initially be locked together lie a three-dimensional jigsaw. Plate impact experiments [7, 13, 28] give clear evidence that this material exhibits a finite shear strength for some time after the initial impact although the spall strength is zero [29-31].

With dynamic loading, it is generally accepted that materials have a limiting crack velocity, less than the Rayleigh (surface) wave speed c_R, since new surfaces are formed in the fracture process [11, 32, 33]. However, in reality the maximum crack velocity does not reach c_R. This may relate to the fact that the velocity of stress waves could be modified in the region of the crack tip by the large stresses found there, and also to cracks initiating ahead of the main crack. Initially these micro-cracks will be overtaken by the main crack. They then manifest themselves as fracture surface roughening (termed 'mist' and 'hackle'). Eventually, if the stress intensity of the fracture front continues to increase, a secondary crack can initiate far enough ahead of main front to reach the main crack velocity. At this stage, crack branching takes place [11]. The combined effects of micro-crack initiation, surface roughening and branching cause the overall crack velocity to level off, perhaps because of the increase in the number of new surfaces to be formed. The practical limiting velocity for a single crack in glasses turns out to be closer to half of the Rayleigh wave speed [11]. Thus we might expect to see one or more cone cracks form at the nose of the rod and travel at a speed of *ca.* 1.8 mm μs^{-1} or less through the pyrex, which is what was observed. However, it should be noted that the above considerations applied to single crack propagation rather than an entire fracture front, which should propagate even more slowly due to the larger surface area created for each increment of crack growth. Also, for cracks diverging from the impact point, it is actually a projection of the cracks which is recorded on the film, rather than the velocity in the direction of propagation of the crack surface. Recently, cracks have been found in certain circumstances to travel faster than this but only at interfaces between two materials [16, 34, 35].

Early on in the impact process, the radius of the contact area between the rod and target expands more rapidly than compressive waves in the steel can travel [36], precluding the possibility of release waves and leading to high compressive pressures as a volume of steel at the end of the rod is compressed. This mode of loading is roughly planar since the rod nose is flattened. The pressure achieved during this brief time may be roughly calculated as the product of the density ρ, longitudinal wave velocity c and impact velocity V [37], except that both projectile (mild steel) and target (pyrex) materials must be taken into account as neither is perfectly rigid (see equation 1):

$$P \approx V \frac{\rho_P c_P \rho_T c_T}{\rho_P c_P + \rho_T c_T}, \quad (1)$$

where ρ_P and c_P relate to the projectile and ρ_T and c_T relate to the target. Using a target density of 2230 kg m^{-3}, a target wave velocity of 5.7 mm μs^{-1} (measured above), a projectile density of 7818 kg m^{-3} and a projectile wave velocity of 5913 mm μs^{-1} gives an approximate value for the initial impact pressure for the two experiments reported above of 5.3GPa. This compares well with the longitudinal stress of 5.2GPa measured in a plate impact at the higher velocity of 650 m s^{-1} [5]. However, the radius of the region subjected to this level of stress, given by rV/c where r is the radius of curvature of the penetrator [9], is only 0.5mm. Therefore this initial phase of loading is short-lived and confined to a small area, although it may lead to significant compaction directly beneath the impact site as in the first few frames of figure 2 where the material within the visible shock wave appears darker. Altered moduli in this zone might contribute to the flattening of the spherical fracture which occurs between 1 and 1.5 μs in figure 2.

2.3 Flash X-ray studies

A 150kV single-shot flash X-ray tube was used to study experiments similar to those discussed above. In order to ensure precise triggering of the X-ray tube, the pyrex blocks were equipped with an impact sensor on the front face. The impact sensor consisted of a double layer of brass shim separated by a layer of adhesive tape. Electrical connections were made to each layer so that when the projectile penetrated through the insulating adhesive layer, a short circuit was made which was sensed by a delay generator. The necessity of adequate contrast between the rod and the glass limited the thickness of the pyrex blocks in the direction of the X-rays to 30mm. So the dimensions of the blocks used were 60mm x 30mm (X-ray path) x 20mm (impact path). X-ray film was loaded in a reinforced cassette the other side of the specimen to the X-ray tube. The block dimensions mean that the lateral inertial constraint is not the same as for the high-speed photographic study neither was it symmetric, but this made minimal difference to the phenomena occurring during the first few microseconds that were recorded using high-speed photography because release waves from the free surfaces would not yet have interacted with the fracture front in the field of view.

Figure 3 presents radiographs from four similar experiments performed at approximately 535 m s^{-1}. The delay time after impact was varied for each shot using a delay generator. Part of figure 3*a* is reprinted as figure 4 with contrast altered to maximise the visibility of the cone crack.

Figure 3. Near here

Figure 4. Near here

The braided electrical contacts for the impact sensor can be seen in each frame. In the fourth radiograph (figure 3*d*) a screw can be seen attached on the side of the rod. This was initially positioned 40mm the rod nose to act as a fiducial mark so that any rod erosion or shortening could be quantified. The glass blocks were glued onto brass mounting brackets which can be seen on either side of the rod. The hemispherical-nosed rod has only penetrated about 1mm into the block by 2.8μs (figures 3*a* and 4), flattening considerably in the process. High-speed photography showed that the fracture front has travelled more than 5mm into the glass by this time (see figure 2). The time the rod 'dwells' on the surface is governed by the development during impact of both materials i.e. the times taken for (i) the glass block to fail completely, (ii) the decrease of stress in the rod as it deforms laterally ('mushrooms') spreading the load over a larger area, and (iii) the time taken for the crushed glass to move aside. These processes overlap in time.

The half-angle of the cone (just) visible in figure 4 is 57˚±1˚ on the left and 53˚±1˚ on the right giving an included angle of 110˚. This figure is within the range of values for dynamic loading reported in the literature e.g. ref. [21]. The left-hand crack originated from a point on the surface about 3.8mm from the impact axis while on the other side the crack projects back to a point 4.4mm from the axis. The most probable explanation for this is that a ring crack nucleated at 3.8mm or less from the axis and then propagated around the circumference of the rod during which time the contact radius also increased.

Figure 3*b* presents the result of an experiment where the delay between the impact and the X-ray flash was 30μs. The rod still dwells in a crater about 6mm deep (the material that was in the crater having been ejected) corresponding to an average penetration speed up to this point of 184 m s^{-1}. The rear surface of the borosilicate can be seen to be bulging by about 3.5mm. The glass block was wholly comminuted by this stage, multiple transits of

the block by both longitudinal and transverse waves having occurred. However, the glass still seems to provide some resistance to penetration and, on the basis of results from plate impact experiments [7], probably retains some shear strength. The rod 'mushroom' is about 21.5mm in diameter, which corresponds to a lateral plastic strain of more than 100%. The steel appears to be flowing outwards and backwards as assumed in Tate's theory [38, 39]. The rod is deforming laterally further down its length as well. Faint fissures can be seen within the comminuted glass (indicated by arrows) parallel to the front surface at a depth of about 3.5mm. Another fissure (also indicated by an arrow) can be seen running at an angle of 55˚ to the impact axis part of the way between the back surface and the deformed rod. Tsai and Chen [40] studied the effects that the distance between the mounting brackets has on whether a glass block fails by Hertzian cone fracture in the impact surface or by cracking due to flexure of the rear surface. However, the original cone crack seen in figure 4 has probably been obliterated by 30μs due to comminution.

The movement of blocks of comminuted glass can be seen to continue in figure 3*c* confirming the tendency of such damaged material to 'lock' together. Note that the pattern of fissures seen in figures 3*b*, 3*c*, and 3*d* are very similar confirming they are reproducible. The lateral fissures at a depth of 3.5mm and roughly parallel to the impact surface continued to extend out from the deforming rod, as did the angled fissures (half-angle 53˚ on left, 63˚ on right, 116˚ inclusive) from the mushroom to the bulging rear surface. Between 30μs and 40μs the rod only advanced another millimetre into the glass (assuming reproducibility between shots) giving an average penetration speed of *ca.* 100 m s^{-1} for this intermediate stage. The mushroomed head of the rod does not appear to have expanded significantly laterally during this time. Roughly half of the apparent penetration by the rod can be accounted for by the bulging of the back surface i.e. movement of material in front of the penetrator due to lack of confinement. Debris continues to be ejected from the impact surface.

The final stage of penetration at 80μs is shown in figure 3*d*. The failure trends of the glass block continue but there is a significant development in the penetrator: the side lobes of the 'mushroom' have sheared off giving a much more streamlined profile for penetration ('self-sharpening'), and the average speed of penetration has risen dramatically to 475 m s^{-1} in the period since 40μs after impact. At least part of the reason for the rapid penetration at this stage is the reduced diameter of the channel through which the rod is

trying to move, being only half of the value at 30μs and 40μs and roughly the same as the initial rod diameter. The comminuted glass may be losing strength as well. Measurement of the distance of the marker screw from the rod nose shows that the rod has shortened by about 10mm due to the shearing off of the lobes and plastic deformation of the rod further back. Some glass fragments can be seen being ejected from the rear surface as the rod breaks out. The lateral and angled fissures seen at 30μs and 40μs persist at similar angles and positions. The block can also be seen beginning to detach from the brass mounts to which it was glued.

In summary, the dwell time was found to be somewhere between 40μs and 60μs, indicating a high degree of resistance to penetration by borosilicate glass, even after comminution. It is also noticeable how the comminuted glass broke into coherent blocks of interlocked fragments, the fissures delineating them being reproducible between experiments (compare figures 3b and 3c). Penetration efficiency is increased considerably where self-sharpening occurs.

Experiments were also performed at oblique impact. Figure 5 presents radiographs from three such experiments, again consisting of mild steel rods impacting upon borosilicate glass blocks of the same dimensions as before at *ca.* 530 m s^{-1}, but this time at an angle of impact of 45˚. The blocks were mounted upon PMMA brackets. Marker screws were again situated in the rods at 40mm from the nose.

Figure 5. Near here

The first radiograph was taken 40μs after impact. Relatively little penetration (7mm normal to the glass surface) had occurred by this time. It would appear that the mild steel rod was deflected away from the impact direction quite early on during the impact since the nose is not very flattened. The bending has the effect, like mushrooming during normal impact, of spreading the load over a wide area as well as creating significant frictional forces between the rod and the glass.

The steel rod shown in figure 5*a* has undergone some lateral deformation in the contact area. Fine ejecta can be seen leaving from the impacted face, particularly to the front of the rod nose as it create an impact crater. The rear surface has also begun to bulge. No cone cracks or fissures are visible in any of these radiographs: this is a marked difference from the normal impact case. There also appears to be no movement of blocks of

interlocked comminuted glass within the target. It is possible that a radiograph taken very early on in the process (say 3μs) might have shown cone crack formation as with the studies by Chaudhri & Chen [18] of oblique impact of glass blocks by spheres, but any such features have been obliterated by 40μs, if they ever existed.

Figure 5*b* shows more of the rod bending into the plane of the glass front surface. The nose of the rod is beginning to curve back on itself, ejecting more glass, and is being flattened. Lateral deformation of the rod appears minimal. We conjecture that most of the impact energy is being dissipated by bending of the rod, flattening of the nose and side, and frictional heat. The rear surface of the glass appears to be moving out as a fine debris normal to the surface behind the broad sweep of the curved rod which has by now advanced normally into the block by 11.5mm, which is over half the initial thickness. The bulk of the ejecta can be seen emerging normal to the surface and to the left of the impact axis because this is where there is the least confinement. The marker screw (on the right side of the rod) has just reached the pyrex front surface.

In the final radiograph (80μs) the same processes continue, with the rod nose turned by about 90˚. Glass which has not been dislodged can be seen behind and in front of the crater. Although the curved section of the rod has penetrated some 17.5mm normally into the originally 20mm thick block, the material that is being pushed ahead and out of the rear surface gives the illusion that there is still a significant fraction of the block still to be penetrated.

Comparing figures 3 and 5, it can be seen that the penetration time for oblique impact on glass is longer than for normal impact. There are several competing factors which have an influence on this: (i) in the normal impact case the mushrooming of the rod initially slows the penetration down but then the penetration speeds up during the self-sharpening phase; (ii) the path length though an oblique target is longer; (iii) rod bending in oblique impact slows the rate of penetration like mushrooming does for normal impact by increasing the cross-section of the rod and by dissipating energy in friction and penetration parallel to the glass surface. The average penetration speeds for the time periods 0-40 μs, 40-60 μs and 60-80 μs in the oblique impact were 175, 225 and 300 m s^{-1} respectively, reflecting the decrease in confinement as the rear surface moves away.

2.4 Fine grid studies

The third technique used in this impact study of borosilicate glass was the observation of the rear surface during penetration using the fine grid technique described in an earlier paper [41]. Figure 6 presents a high-speed photographic sequence, lasting 16.5 μs, of the 532 m s^{-1} impact of a round-nosed mild steel rod onto a 9.5mm thick borosilicate glass block. As before the first frame was triggered by one of our brass shim impact sensors. The grid lines are spaced 1mm apart and the grid is illuminated at an angle from the left side (figure 7).

Figure 6. Near here

Figure 7. Near here

A single-transit of the target by a longitudinal elastic stress wave should take 1.7μs while an elastic shear wave will take 2.6μs. We might therefore expect to see, and in fact do see, the first signs of damage to the rear surface in the third frame when both waves have arrived at and been reflected from this free surface. Initially a disc-shaped region (plug) of approximately the rod diameter (10 grid lines) can be seen moving out from the surface having a fairly jagged periphery but with little grid distortion in the centre of the plug of material. By 9μs a larger area of deformation becomes visible. This will be when the transverse wave will have returned for the second time, encompassing much of the field-of-view as it develops. The centre of the region of impact remains largely undeformed. It is possible, but not certain, that the larger area is the base of a Hertzian cone. Such a cone would be *ca.* 24mm across at the rear surface if it had an internal half-cone angle of 55˚ (typical of sphere impacts on glass [14, 18, 21, 42]). The cone cracks would also reach the rear surface at around 5 μs.

It is not possible to quantitatively compare the rear surface deformation with that seen in the X-radiographs because of the difference in target thickness, but we can use the understanding of the dynamic behaviour of the glass gained using X-rays. For example, we saw that the comminuted glass moved as blocks of interlocking fragments, and this is consistent with the jagged edges seen late on in the sequence as is the relatively small amount of distortion seen in the central plug section. Also, at 10.5μs (frame 8) we see a diagonal crack across the central region visible as a discontinuity in the grid. This is we

interpret as one block of glass having advanced further than its neighbour. This discontinuity disappears at later times, presumably because the two blocks had now reached the same displacement and were advancing in step.

3. Numerical modelling

There are some significant challenges involved in the modelling of these experiments, particularly concerning the 'dwell' effect. A key requirement for a model is a mechanism to account for the time-dependence of failure and flow in a heavily damaged medium at high strain rates.

The brittle model due to Goldthorpe and co-workers [43] used in these analyses was constructed directly from plate impact experiments on brittle materials such as various glasses and alumina ceramics and is phenomenologically based on the behaviour of 'failure waves' (or more accurately failure fronts) observed using manganin stress gauges in the longitudinal and lateral configurations[28, 44] (see figure 8).

The time interval between the rise in the longitudinal stress and the 'jump' in the lateral stress gauge record is indicative of a failure front (or wave) as reported elsewhere[44].

Figure 8. Near here

Since plate impact generates uniaxial strain, the shear stress can be calculated using the following equation:-

$$2\tau = \sigma_y - \sigma_x \qquad (2)$$

where σ_y is the longitudinal stress, σ_x is the lateral stress, and τ is the shear stress.

The shear stress for brittle materials can be used to measure their failure strength (akin to yield in ductile materials). The use of both longitudinal and lateral stress gauges allows this parameter to be measured fully experimentally.

Plate impact tests on brittle materials such as glass and ceramics show some important similarities to experimental data on metals. In particular brittle materials usually show a longitudinal wave as a precursor to the main shock wave. The transition from a longitudinal elastic to a plastic front requires that the brittle material has the ability to

'flow' in a manner analogous to that observed in ductile materials. It is principally this characteristic which forms the basis for the construction of a flow model.

In order to incorporate all of the above effects into a general model it is assumed that on impact the brittle material must break up into an aggregate before it can flow. Also the degree of fragmentation will influence the ease with which it flows. This process is represented by either of the curves in figure 9. These show that at some value of the deviatoric stress, deformation or flow can commence. As the deviatoric strain increases the comminution will also increase and the strength will fall. This reaches an end point for the test conditions which is the strength normally observed at the back of the shock wave and is used to construct the $\overline{\sigma}$ vs. pressure curve. The form of the model is thus quite simplistic with the criterion that the material cannot flow until it damages and can thereafter accommodate plastic strain.

Figure 9. Near here

If the waves are divergent, the rate of compression across the wavefront will decrease as the wave propagates through the target. Thus there will be a strain rate variation which would be expected to influence the flow rate. This would produce a higher stress near the impact face (curve 2) compared to stresses further into the target (curve 1).

The simplest equation or model to describe these effects is:-

$$\overline{\sigma} = A + B\dot{\varepsilon}^{m} + C\overline{\varepsilon} \qquad (3)$$

where $\overline{\sigma}$ is the effective stress, $\dot{\varepsilon}$ is the strain rate, $\overline{\varepsilon}$ is the deviatoric plastic strain, and A, B, C, m are constants.

There are a number of limitations to this model. Firstly the material needs to be in an initial state of failure with a continuous network of cracks before the material can flow. This may require a plateau or other modification to figure 9 to provide a more accurate representation. Secondly the simple linear model used is primarily governed at this stage by the difficulty of obtaining accurate data across the shock front. Another important limitation is the lack of progression from damage through to macroscopic cracking of the material, other than by linkage to a simple spall strength. All these areas are currently

being investigated for brittle materials within QinetiQ using a new approach developed by Porter and Gould based on Quantitative Structure Property Modelling[45-47].

In spite of these limitations the Goldthorpe brittle model is an elegantly simple attempt to model the impact behaviour of brittle materials. The phenomenon of precursor decay can be readily demonstrated. Also the more difficult problem of dwell is understandable since the model shows the need to produce damage before the material can flow. Thus projectile penetration can only commence after the damage has occurred and after it has started to propagate, usually as a failure front, into the target. The dwell period produced by these effects will decrease with impact velocity because the wave divergence decreases with the increase in pressure produced by higher impact speeds. Clearly both strain rate dependence and 'plastic strain' are essential variables in controlling the complete process.

Despite the simplicity of the model it is still very difficult to obtain data for the constants for equation (3). The main reason for this is that the model depends on measurements of the longitudinal and lateral stress 'pairs'. This causes some difficulty experimentally since the temporal and spatial resolution of the longitudinal and lateral gauges are different and hence it is not straightforward to accurately align the gauge traces. This is crucial particularly for the calculation of the strain rate exponent, where the impact experiment needs to produce matching longitudinal and lateral stress pairs. A further difficulty is the recent concerns regarding the validity of the stress measurements using the lateral gauge[48]. As a result of these issues the present approach is to fit the model parameters to the longitudinal and lateral stress pairs shown in figure 8 (see Table 2*a*). The resulting parameters are then used to predict the penetration experiments reported earlier.

Table 2 near here

3.1 Simulation results

The simulations were performed using the QinetiQ Eulerian hydrocode GRIM, which features multi-material options and sophisticated interface options and is well suited for penetration simulations[49]. Some simulations were also performed using the public domain version of the Lagrangian hydrocode DYNA3D for comparison. The Goldthorpe brittle model was very easy to implement and behaves in a robust fashion, such that it readily converges as the mesh size reduces. The equation of state used was a standard Mie-Grüneisen for the appropriate form of glass (see Table 2*b*).

The penetration experiments were simulated to test the model's ability to reproduce dwell at a given low velocity and then to determine whether the model would predict penetration at a higher velocity. The mild steel rod was simulated using a modified Armstrong-Zerilli model[50]. The glass block was simulated using the model just described in this paper.

An example plot of the interfaces for the normal impact at a velocity where dwell is significant is shown in figure 10.

Figure 10 near here

Figure 11 near here

It can be seen that at the lower velocity a significant portion of the penetrator is being consumed on the surface of the target. The results for both DYNA and GRIM in this and other scenarios were very similar indicating that the numerical scheme was having little influence on the results. Furthermore this behaviour was exhibited for all the mesh resolutions studied indicating that the model is not particularly mesh sensitive and is also very robust. Increasing the velocity caused the mild steel rod to penetrate the target (figure 11) and also allowed the rod to 'mushroom' as was observed in the flash radiographs (figure 3). This demonstrates that the model is capable of predicting the transition from the rod being consumed at the surface to the rod penetrating the target. However, it is clear that the model will not predict the detailed crack patterns observed in the experiments, highlighting the need for a physically based transition from damage to fracture in the model.

A more stringent test of the model was the simulation of an oblique impact. Again at the lower velocity the rod is consumed and bends at the target surface (figure 12), whereas at higher velocity the rod starts to penetrate the target (figure 13). It is encouraging that the simulation predicts the observed bending of the rod (compare with figure 5). This shows that the model works extremely well in 3D and produces the dominant phenomenology.

Figure 12 near here

Figure 13 near here

These results are very encouraging for what is a very simply based model and allow its use for scoping studies for designing potential armour systems, for example. Clearly further work is required to understand the precise limitations of the model.

4. Conclusions

High-speed photography, X-radiography and the fine-grid optical technique gave significant information about the ballistic impact properties of borosilicate glass. At the impact velocities studied, the glass rapidly becomes heavily comminuted, but still exhibits Hertzian-type cone failure as well as stress wave damage. The fracture front is not coupled to the expanding shock wave as it would be (on the basis of plate impact studies) at higher velocities. The comminuted material still retains strength and this, with the flattening of the rod nose, gives a significant 'dwell' time. The rod slows as it produces a mushroomed head but speeds up as the mushroom head is lost and the rod sharpens. The comminuted material fails in blocks, the pattern of which was found to be reproducible shot-to-shot. These results were compared with numerical simulations made using a physically based model of the behaviour of brittle materials under shock loading which had previously been shown to reproduce experimentally observed precursor decay and failure wave behaviour. The model was able to qualitatively predict the transition from dwell to penetration of a glass target. This approach developed for sodalime glass should be equally applicable to ceramics and concrete and other brittle materials. The model converges on the mesh and is very robust in both Eulerian and Lagrangian hydrocodes.

Acknowledgements

The research reported in this paper was funded by the Defence Evaluation and Research Agency (DERA) now QinetiQ. We would also like to thank past and present members of the Cavendish Laboratory's mechanical and electronic workshops for assistance with the design and construction of apparatus and specimens required for these experiments. LCF was supervised initially by Dr (now Professor) N.K. Bourne before his move to Cranfield University and then by Professor J.E. Field and Dr W.G. Proud.

References

1. Toqueboeuf, W., Mortaigne, B., and Cottenot, C. Dynamic behaviour of polycarbonate/polyurethane multilayer for transparent armor. J. Phys. IV France 1997;7(C3): 499-504
2. Hall, C.W.G., Harper, R.A., and Snelling, J.P. Bullet resistant glazings for automotive vehicles. In Proc. Int. Body Engineering Conference and Exposition. Vol. 3, eds. pp. 332-337. Warrendale, PA, SAE International (1998)
3. Grant, P.V., Cantwell, W.J., McKenzie, H., and Corkhill, P. The damage threshold of laminated glass structures. Int. J. Impact Engng 1998;21: 737-746
4. Walley, S.M., Field, J.E., Blair, P.W., and Milford, A.J. The effect of temperature on the impact behaviour of glass/polycarbonate laminates. Int. J. Impact Engng 2004;30: 31-53
5. Bourne, N.K., Forde, L.C., Millett, J.C.F., and Field, J.E. Impact and penetration of a borosilicate glass. J. Phys. IV France 1997;7(C3): 157-162
6. Millett, J.C.F., Bourne, N.K., and Rosenberg, Z. Direct measurements of strain in a shock-loaded, lead-filled glass. J. Appl. Phys. 2000;87: 8457-8460
7. Radford, D.D. The inelastic behavior and failure of dense glass under shock loading to 15 GPa. J. Appl. Phys. 2005;98: 063504
8. Bourne, N.K., Rosenberg, Z., Johnson, D.J., Field, J.E., Timbs, A.E., and Flaxman, R.P. Design and construction of the UK plate impact facility. Meas. Sci. Technol. 1995;6: 1462-1470
9. Bowden, F.P. and Field, J.E. The brittle fracture of solids by liquid impact, by solid impact and by shock. Proc. R. Soc. Lond. A 1964;282: 331-352
10. Bourne, N.K., Rosenberg, Z., and Ginzburg, A. The ramping of shock waves in three glasses. Proc. R. Soc. Lond. A 1996;452: 1491-1496
11. Field, J.E. Brittle fracture: Its study and application. Contemp. Phys. 1971;12: 1-31
12. Bourne, N.K., Rosenberg, Z., Mebar, Y., Obara, T., and Field, J.E. A high-speed photographic study of fracture wave propagation in glasses. J. Phys. IV France 1994;4(C8): 635-640
13. Bourne, N.K., Rosenberg, Z., and Field, J.E. High-speed photography of compressive failure waves in glasses. J. Appl. Phys. 1995;78: 3736-3739
14. Chaudhri, M.M. and Kurkjian, C.R. Impact of small steel spheres on the surfaces of 'normal' and 'anomalous' glasses. J. Amer. Ceram. Soc. 1986;69: 404-410
15. Radford, D.D., Willmott, G.R., and Field, J.E. The effect of structure on failure front velocities in glass rods. In Shock Compression of Condensed Matter - 2003, M.D. Furnish, Y.M. Gupta, and J.W. Forbes eds. pp. 755-758. Melville NY, American Institute of Physics (2004)
16. Rosakis, A.J., Samudrala, O., and Coker, D. Cracks faster than the shear wave speed. Science 1999;284: 1337-1340
17. Willmott, G.R. and Radford, D.D. Taylor impact of glass rods. J. Appl. Phys. 2005;97: 93522
18. Chaudhri, M.M. and Chen, L. The orientation of the Hertzian cone crack in soda-lime glass formed by oblique dynamic and quasi-static loading with a hard sphere. J. Mater. Sci. 1989;24: 3441-3448
19. Field, J.E. High speed photography at the Cavendish Laboratory, Cambridge. In High Speed Photography and Photonics, S.F. Ray eds. pp. 301-314. Oxford, Focal Press (1997)

20. Knight, C.G., Swain, M.V., and Chaudhri, M.M. Impact of small steel spheres on glass surfaces. J. Mater. Sci. 1977;12: 1573-1586
21. Chaudhri, M.M. and Walley, S.M. Damage to glass surfaces by the impact of small glass and steel spheres. Philos. Mag. A 1978;37: 153-165
22. Hertz, H. Über die Berührung fester elastischer Körper. J. reine angew. Math. 1882;92: 156-171
23. Hertz, H. On the contact of elastic solids. In Miscellaneous Papers by Heinrich Hertz, D.E. Jones and G.A. Schott eds. pp. 146-162. London, Macmillan (1896)
24. Hertz, H. On the contact of rigid elastic solids and on hardness. In Miscellaneous Papers by Heinrich Hertz, D.E. Jones and G.A. Schott eds. pp. 163-183. London, Macmillan (1896)
25. Lawn, B.R. and Wilshaw, T.R. Fracture of Brittle Solids, publ. Cambridge, Cambridge University Press (1975)
26. Field, J.E., Townsend, D., and Sun, Q. High speed photographic studies of the ballistic impact of ceramics. Proc. SPIE 1988;1032: 672-679
27. Field, J.E., Sun, Q., and Townsend, D. Ballistic impact of ceramics. Inst. Phys. Conf. Ser. 1989;102: 387-393
28. Bourne, N.K., Millett, J.C.F., and Field, J.E. On the strength of shocked glasses. Proc. R. Soc. Lond. A 1999;455: 1275-1282
29. Brar, N.S., Bless, S.J., and Rosenberg, Z. Impact-induced failure waves in glass bars and plates. Appl. Phys. Letts 1991;59: 3396-3398
30. Brar, N.S., Rosenberg, Z., and Bless, S.J. Spall strength and failure waves in glass. J. Phys. IV France 1991;1(C3): 639-644
31. Brar, N.S. and Bless, S.J. Failure waves in glass under dynamic compression. High Press. Res. 1992;10: 773-784
32. Swain, M.V. and Hagan, J.T. Rayleigh wave interaction with, and the extension of, microcracks. J. Mater. Sci. 1980;15: 387-404
33. Mott, N.F. Fracture of metals: Theoretical considerations. Engineering 1948;165: 16-18
34. Rosakis, A.J., Samudrala, O., Singh, R.P., and Shukla, A. Intersonic crack propagation in bimaterial systems. J. Mech. Phys. Solids 1998;46: 1789-1813
35. Wu, J. Crack-tip field of a supersonic bimaterial interface crack. Trans. ASME: J. Appl. Mech. 2002;69: 693-696
36. Field, J.E., Lesser, M.B., and Dear, J.P. Studies of two-dimensional liquid-wedge impact and their relevance to liquid-drop impact problems. Proc. R. Soc. Lond. A 1985;401: 225-249
37. Bowden, F.P. and Brunton, J.H. The deformation of solids by liquid impact at supersonic speeds. Proc. R. Soc. Lond. A 1961;263: 433-450
38. Tate, A. A theory for the deceleration of long rods after impact. J. Mech. Phys. Solids 1967;15: 387-399
39. Tate, A. Further results in the theory of long rod penetration. J. Mech. Phys. Solids 1969;17: 141-150
40. Tsai, Y.M. and Chen, Y.T. Transition of Hertzian fracture to flexure fracture produced in glass plates by impact. Engng Fract. Mech. 1983;18: 1185-1190
41. Rae, P.J., Goldrein, H.T., Bourne, N.K., Proud, W.G., Forde, L.C., and Liljekvist, M. Measurement of dynamic large-strain deformation maps using an automated fine grid technique. Optics Lasers Engng 1999;31: 113-122
42. Chaudhri, M.M. and Brophy, P.A. Single particle impact damage of fused silica. J. Mater. Sci. 1980;15: 345-352

43. Church, P., Goldthorpe, B., Cullis, I., and Rosenfeld, D. Development and validation of a dwell model. In Proc. 19th Int. Symp. on Ballistics, I.R. Crewther eds. pp. 1337-1344. Interlaken, Switzerland, (2001)
44. Bourne, N.K., Rosenberg, Z., and Millett, J.C.F. The plate impact response of three glasses. In Structures under Shock and Impact IV, N. Jones, C.A. Brebbia, and A.J. Watson eds. pp. 553-562. Southampton, Computational Mechanics Publications (1996)
45. Porter, D. Modelling of structural materials. Int. Mater. Rev. 2002;47: 225-232
46. Porter, D. Multiscale modelling of structural materials. In Multiscale Materials Modelling: Fundamentals and Applications, Z.X. Guo eds. pp. 261-287. Cambridge, UK, Woodhead Publishing (2007)
47. Cullis, I., Hinton, M., Gilbert, S., Church, P., Porter, D., Andrews, T., Proud, W., and Pullen, A. Towards predictive modelling for concrete. Int. J. Impact Engng 2008;35: 1478-1483
48. Rosenberg, Z., Ashuach, Y., Bourne, N.K., and Dekel, E. On the shock response of soda lime glass: The failure of embedded stress gauges. In Shock Compression of Condensed Matter - 2007, M. Elert, M.D. Furnish, R. Chau, N. Holmes, and J. Nguyen eds. pp. 763-766. Melville, NY, American Institute of Physics (2007)
49. Church, P., Cullis, I., Bowden, A., and Gibson, D. Simulation of the perforation of low mass long L/D rods against finite thickness RHA plates. In Proc. 22nd Int. Symp. on Ballistics, W. Flis and B. Scott eds. pp. 1155-1162. Lancaster, PA, DEStech Publications Inc. (2005)
50. Goldthorpe, B.D., Butler, A.L., and Church, P. A wide range constitutive equation for medium and high strength steel. J. Phys. IV France 1994;4(C8): 471-476

Figure captions

Figure 1. Selected frames from the high-speed photographic sequence of the impact of a 25mm thick, 75mm square borosilicate glass block by a hemispherical-nosed mild steel rod at 531 m s^{-1}. The spacing of the ticks is 5mm. A compressive shock wave can be seen as a curved bright moving from left to right during the sequence. This is followed some distance behind by a black failure front moving more slowly than the shock. The impact face is outside the field of view to the left.

Figure 2. Selected frames from the high-speed photographic sequence of the impact of a 25mm thick, 75mm square borosilicate glass block by a hemispherical-nosed mild steel rod at 536 m s^{-1}. The spacing of the ticks is 5mm.

Figure 3. X-radiographs from four similar experiments involving the impact of round-ended mild steel rods against 20mm thick borosilicate glass blocks at approximately 535 m s^{-1}. The wires that can be seen are electrical contacts to the impact sensor. The fiducial screw seen in frame (d) was located 40mm from the nose of the rod. Visible cracks are indicated using arrows. Times after impact: (a) 2.8μs; (b) 30μs; (c) 40μs; (d) 80μs.

Figure 4. The radiograph that was presented in figure 3a but with the contrast enhanced to show the cone crack formed on impact. The lines at the side indicate the position of the cone cracks.

Figure 5. X-radiographs from three similar experiments involving the 45˚ impact of hemispherical-nosed mild steel rods against 20mm thick borosilicate glass blocks at approximately 530 m s^{-1}. The wires that can be seen are electrical contacts to the impact sensor. The fiducial screws seen in all frames were located 40mm from the nose of the rod. Times after impact: (a) 40μs; (b) 60μs; (c) 80μs.

Figure 6. High-speed photographic sequence of the rear surface of a 9.5mm thick borosilicate glass block being impacted by a hemispherical-nosed rod at 523 m s^{-1}. Grid spacing is 1mm. Impact took place at 0μs.

Figure 7. Schematic diagram of the experimental arrangement used for taking the sequence presented in figure 6. a), b), and c) are front-silvered mirrors. Mirror c) also acts to block the direct light path from the flash to the camera.

Figure 8. Example of longitudinal and lateral stress gauge records for glass (from ref. [28]).

Figure 9. Schematic diagram of stress level as a function of impact stress.

Figure 10. 2D impact low velocity impact simulation.

Figure 11. 2D impact high velocity impact simulation

Figure 12. Oblique impact low velocity simulation

Figure 13. Oblique impact higher velocity simulation

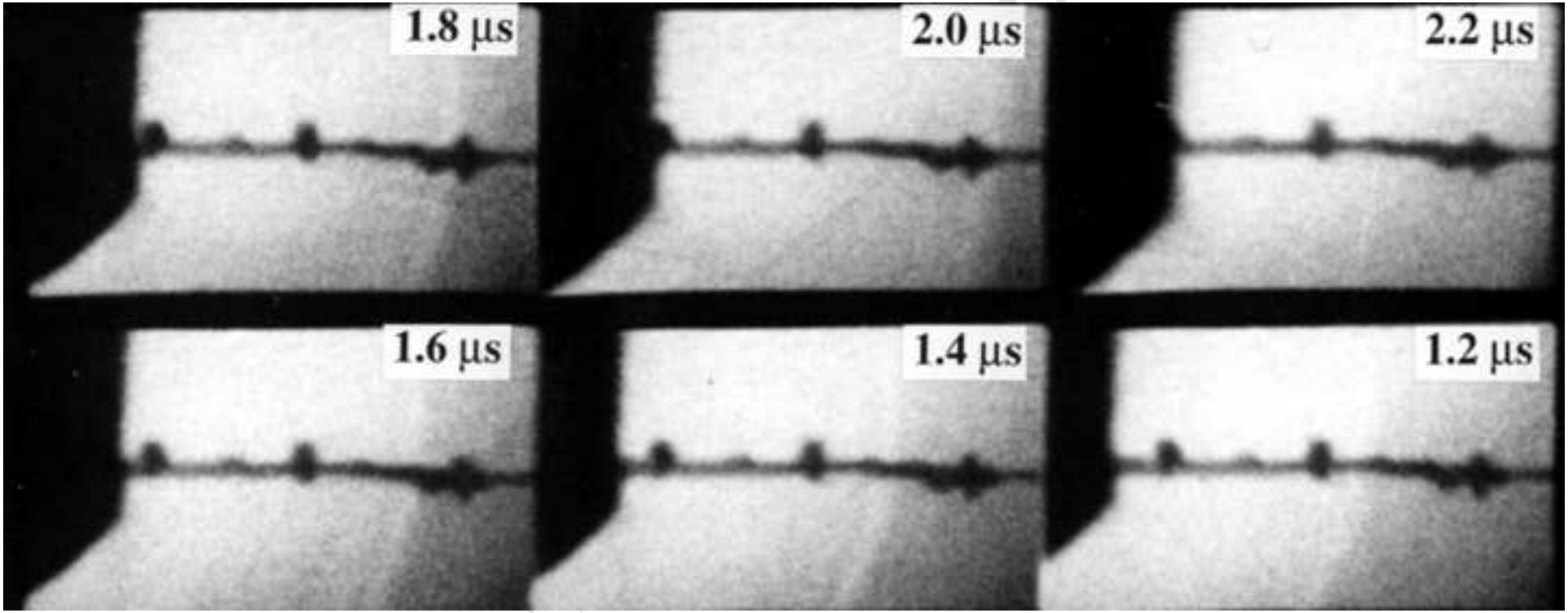

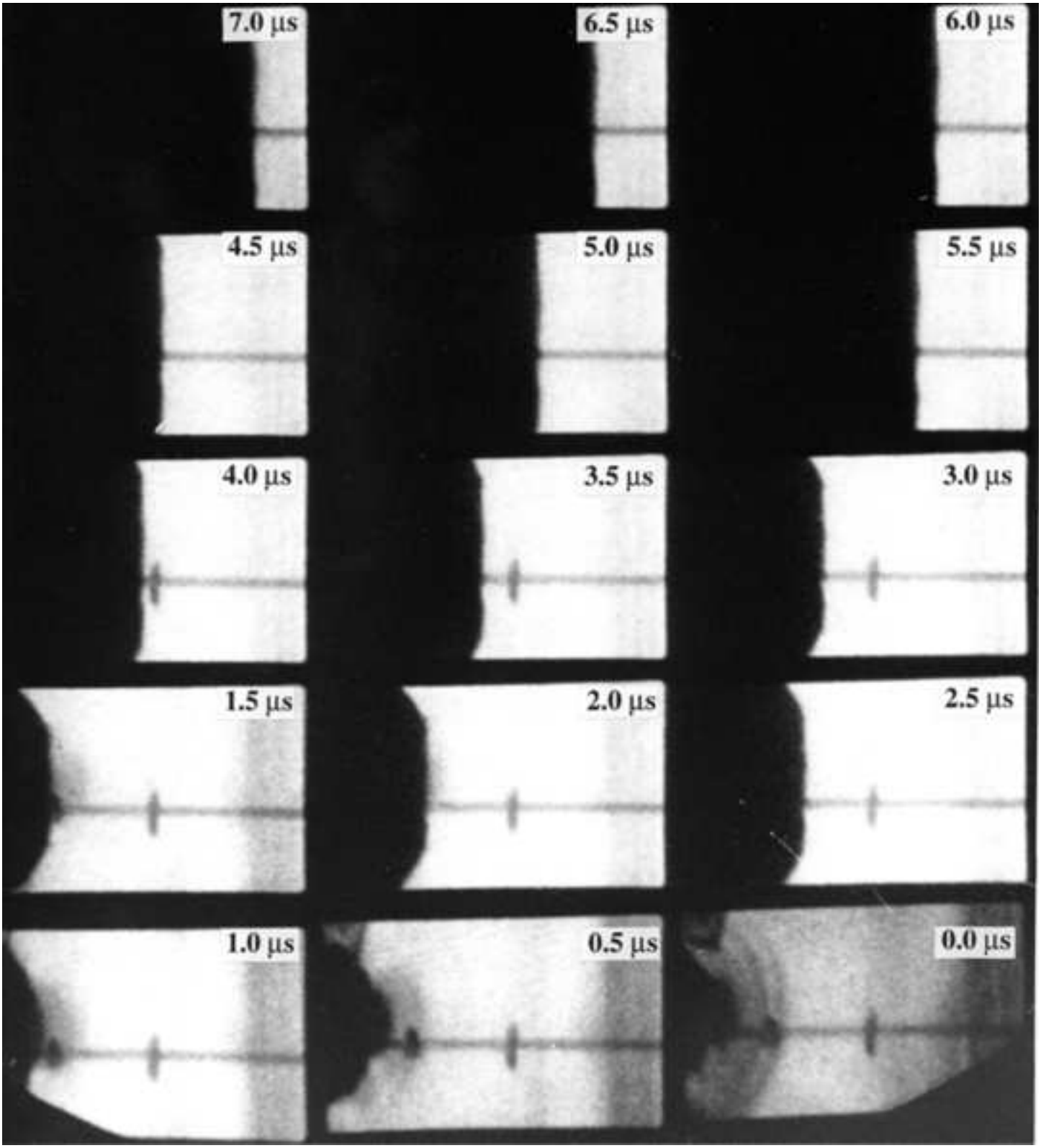
7.0 μs
6.5 μs
6.0 μs
4.5 μs
5.0 μs
5.5 μs
4.0 μs
3.5 μs
3.0 μs
1.5 μs
2.0 μs
2.5 μs
1.0 μs
0.5 μs
0.0 μs

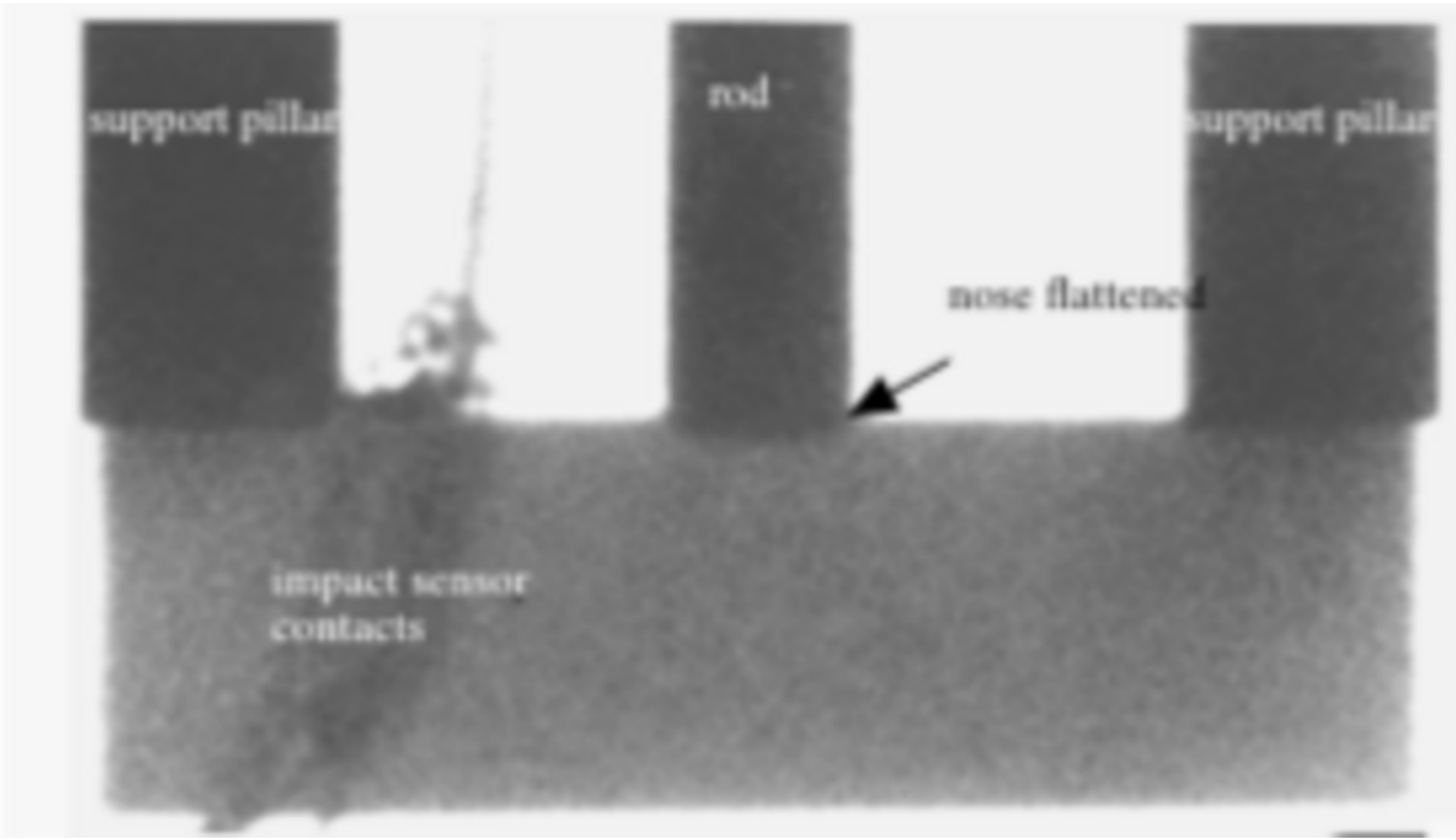
support pillar
rod
support pillar
nose flattened
impact sensor
contacts

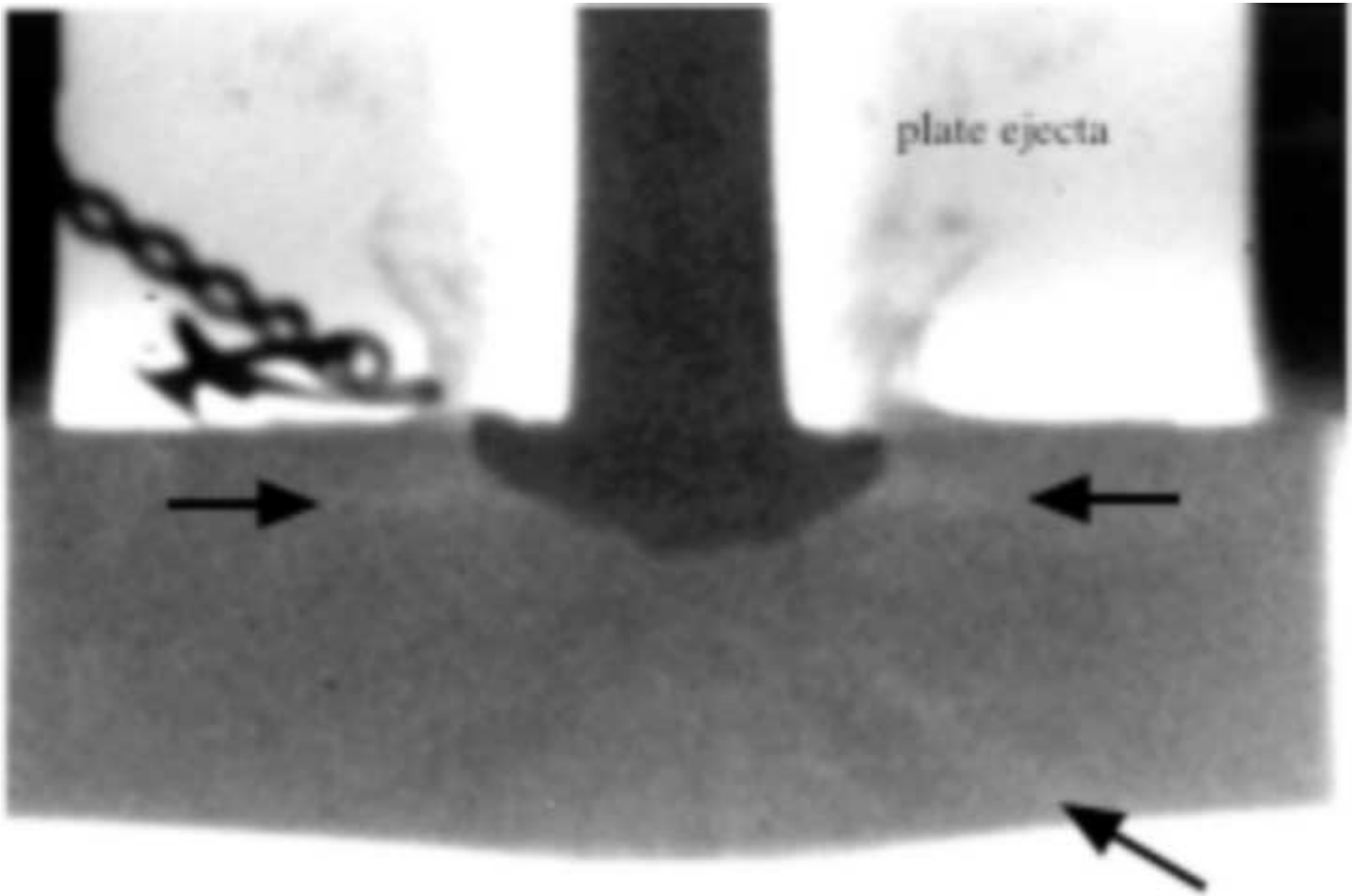
plate ejecta

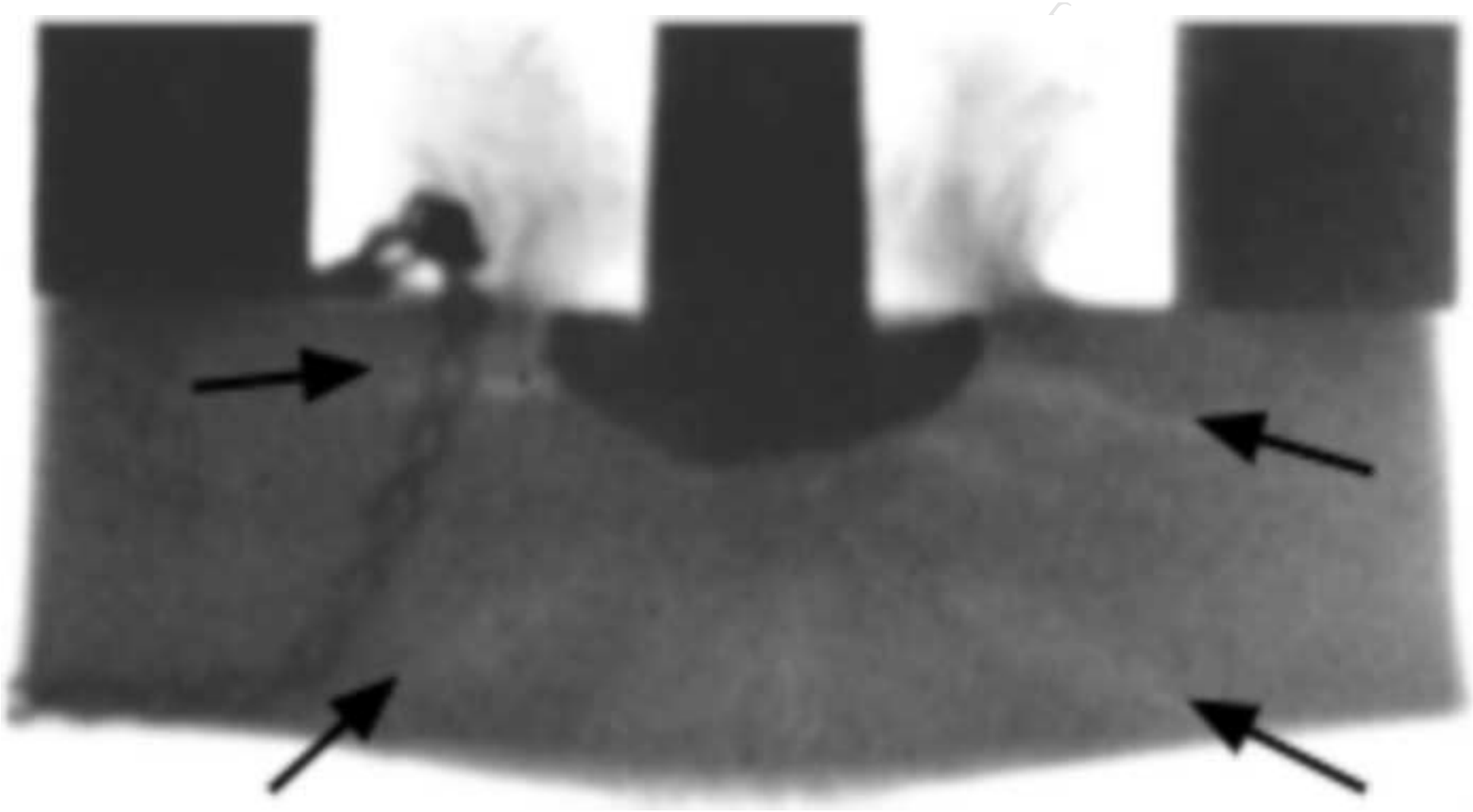

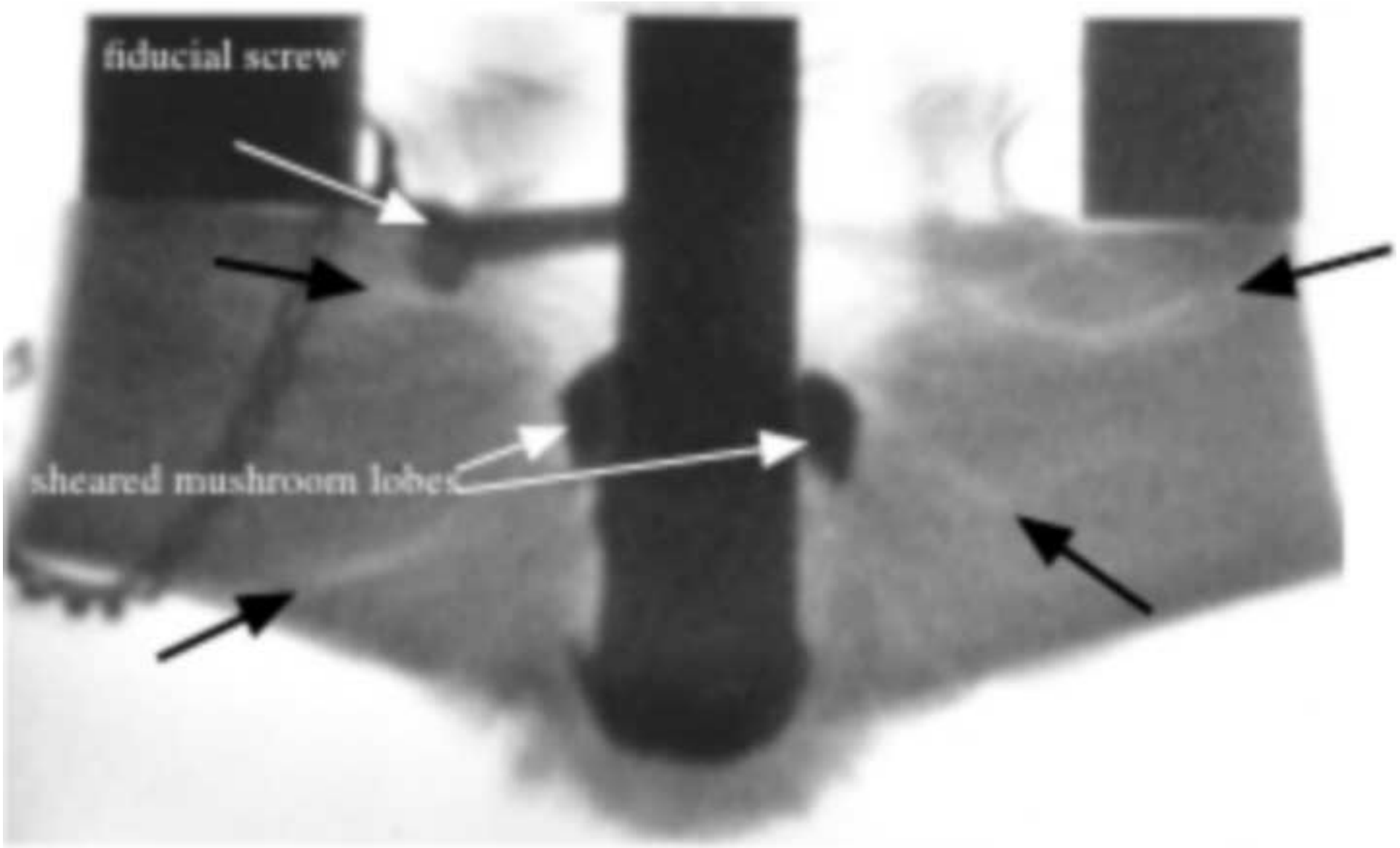
fiducial screw
sheared mushroom lobes

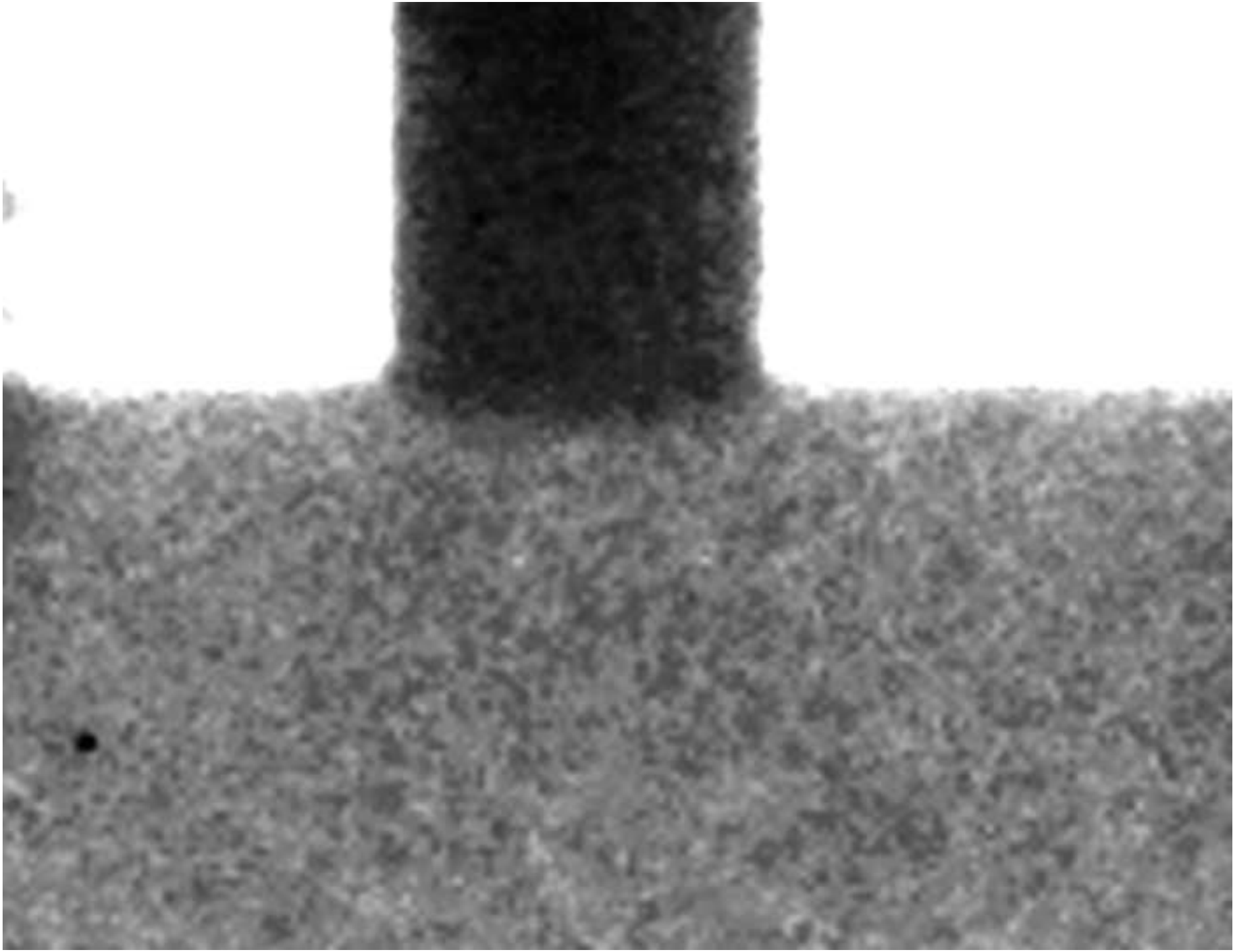

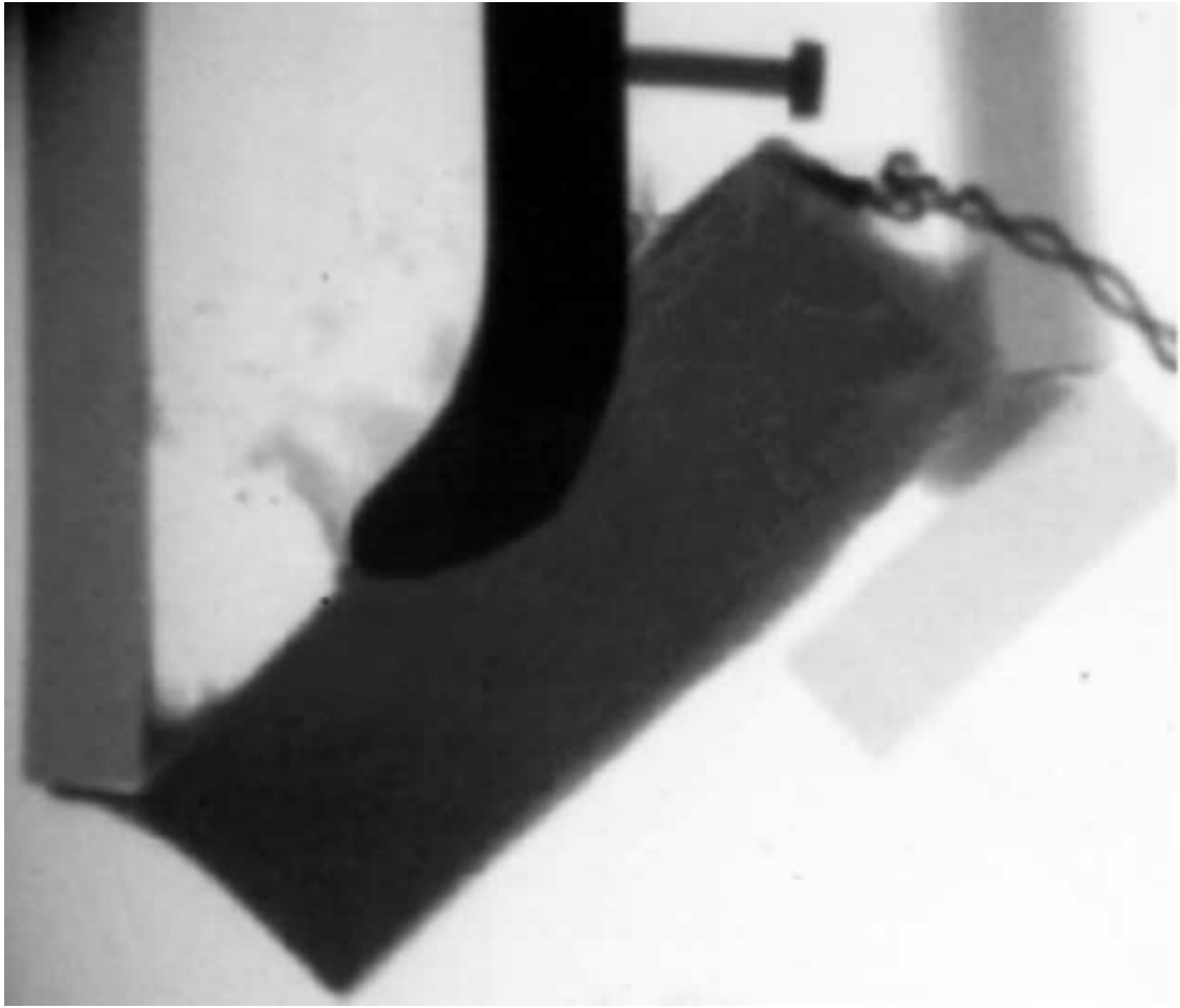

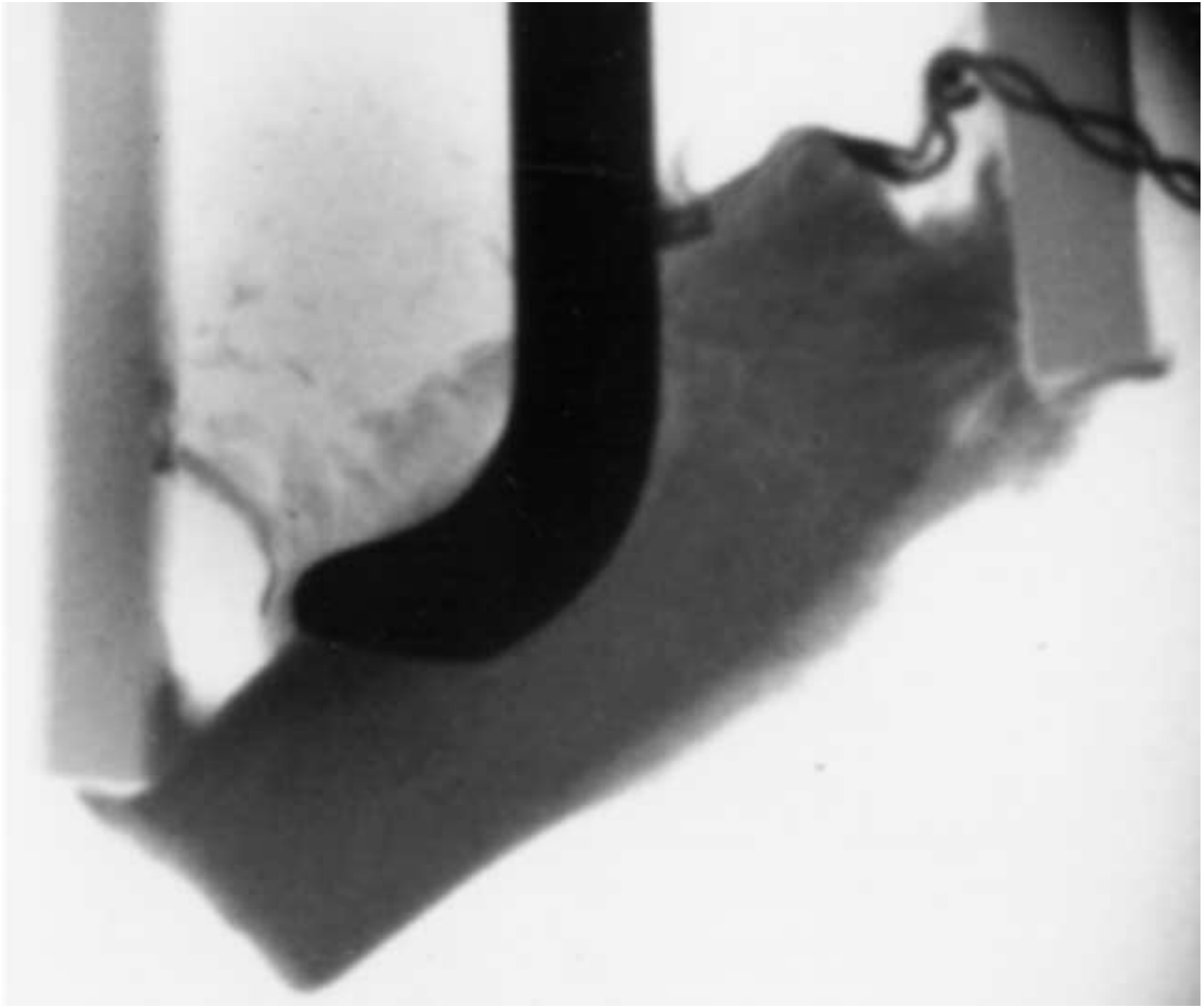

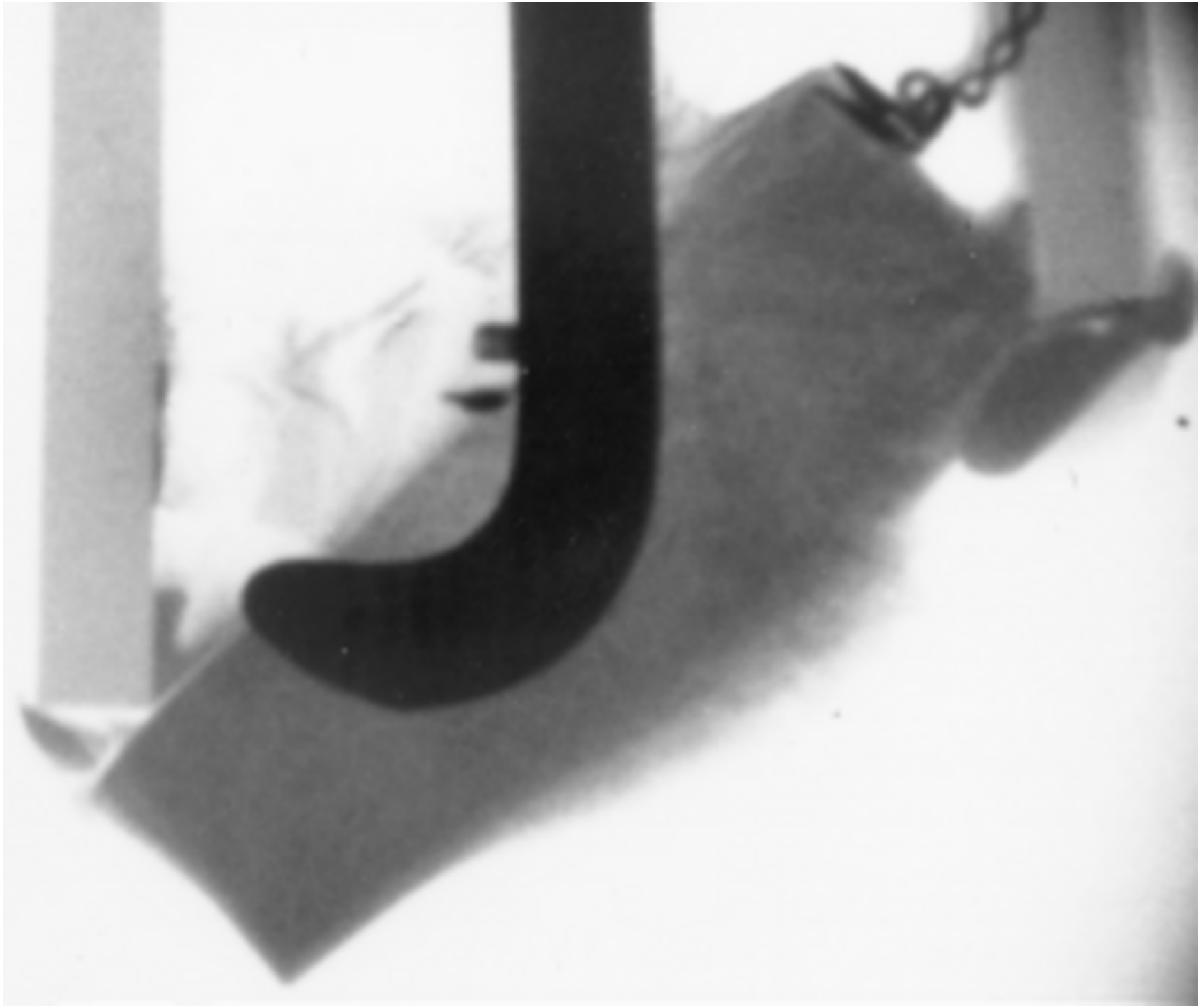

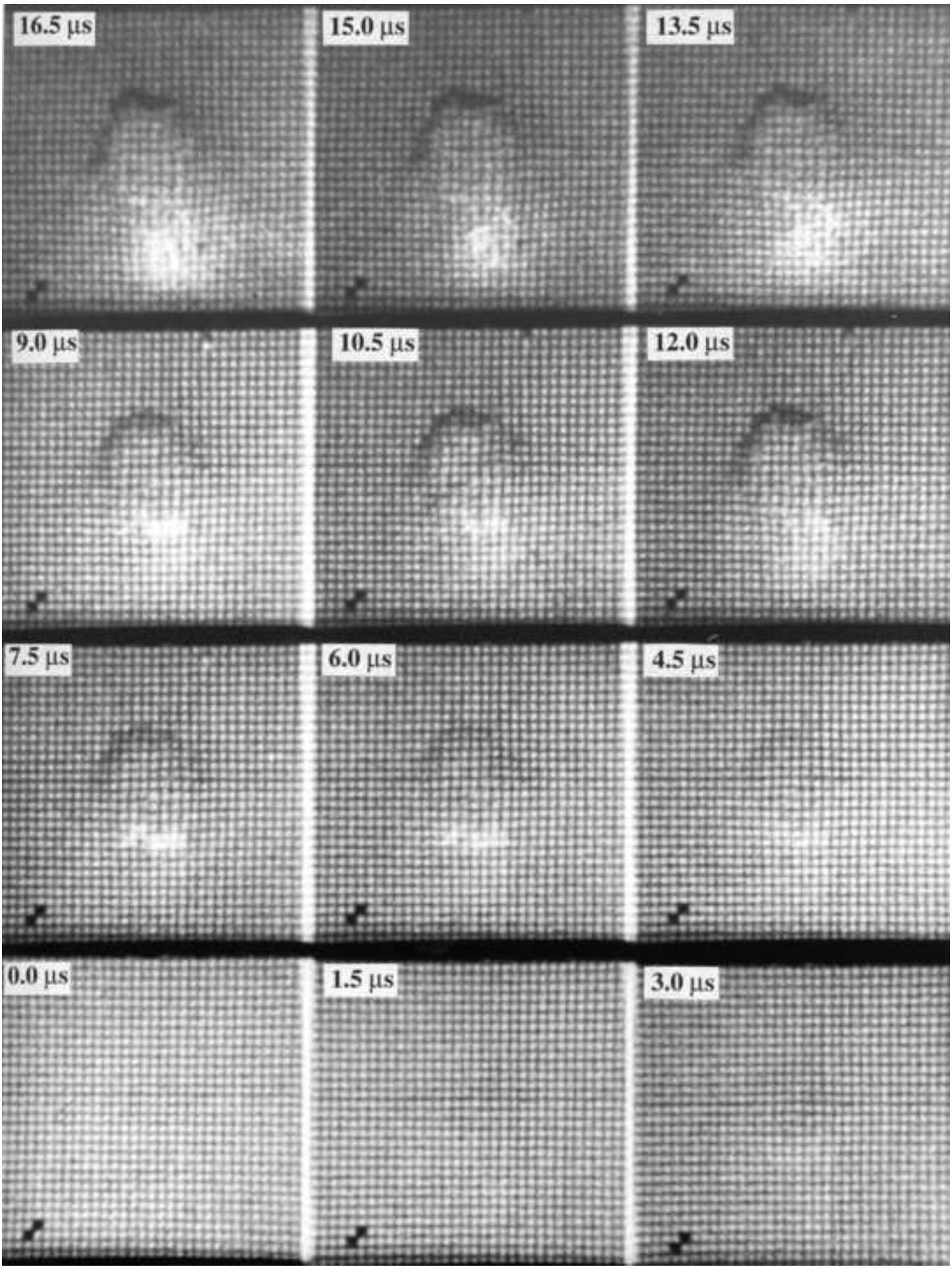
16.5 μs
15.0 μs
13.5 μs
9.0 μs
10.5 μs
12.0 μs
7.5 μs
6.0 μs
4.5 μs
0.0 μs
1.5 μs
3.0 μs

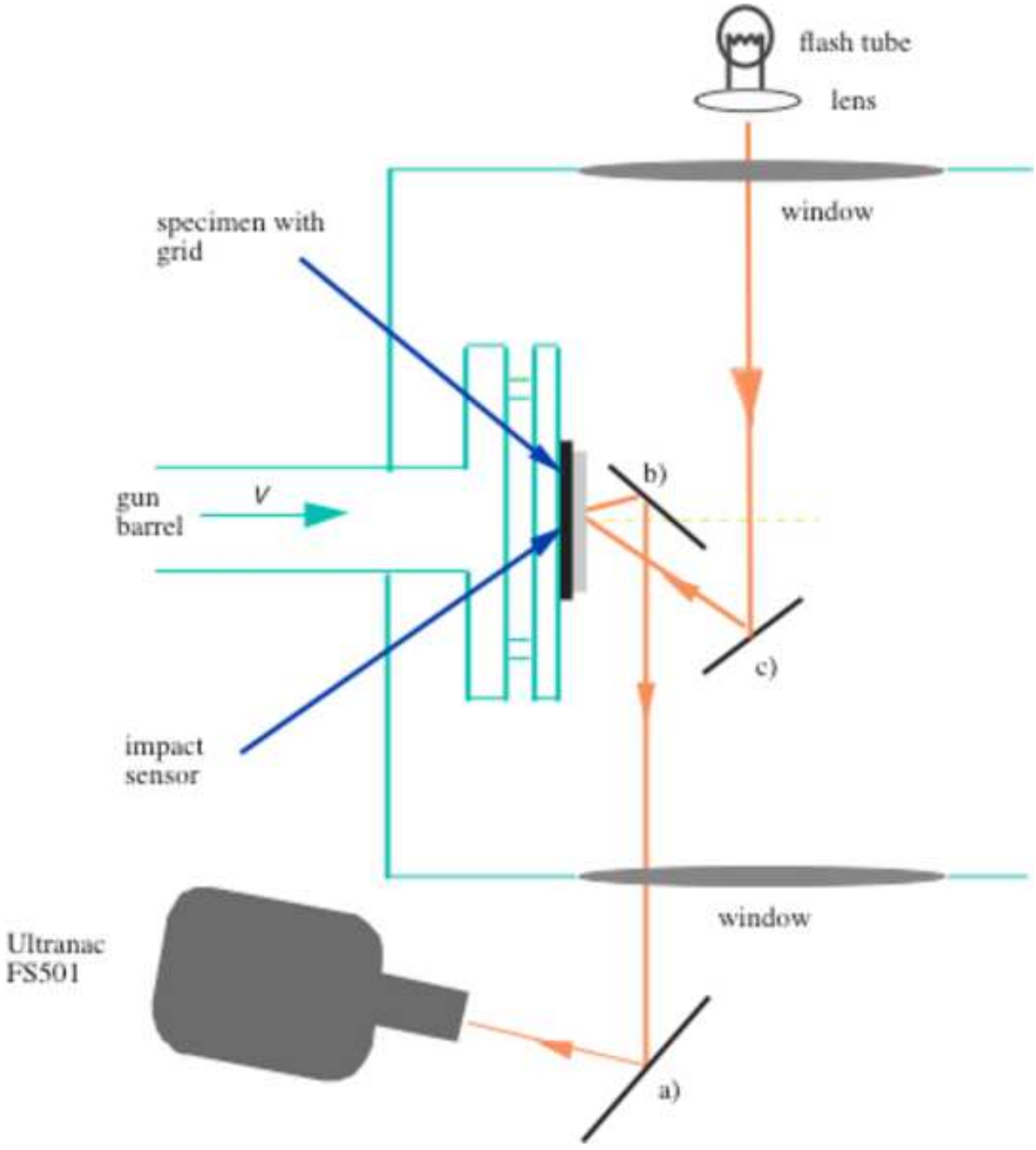
flash tube
lens
window
specimen with
grid
gun
barrel
V
b)
c)
impact
sensor
window
Ultranac
FS501
a)

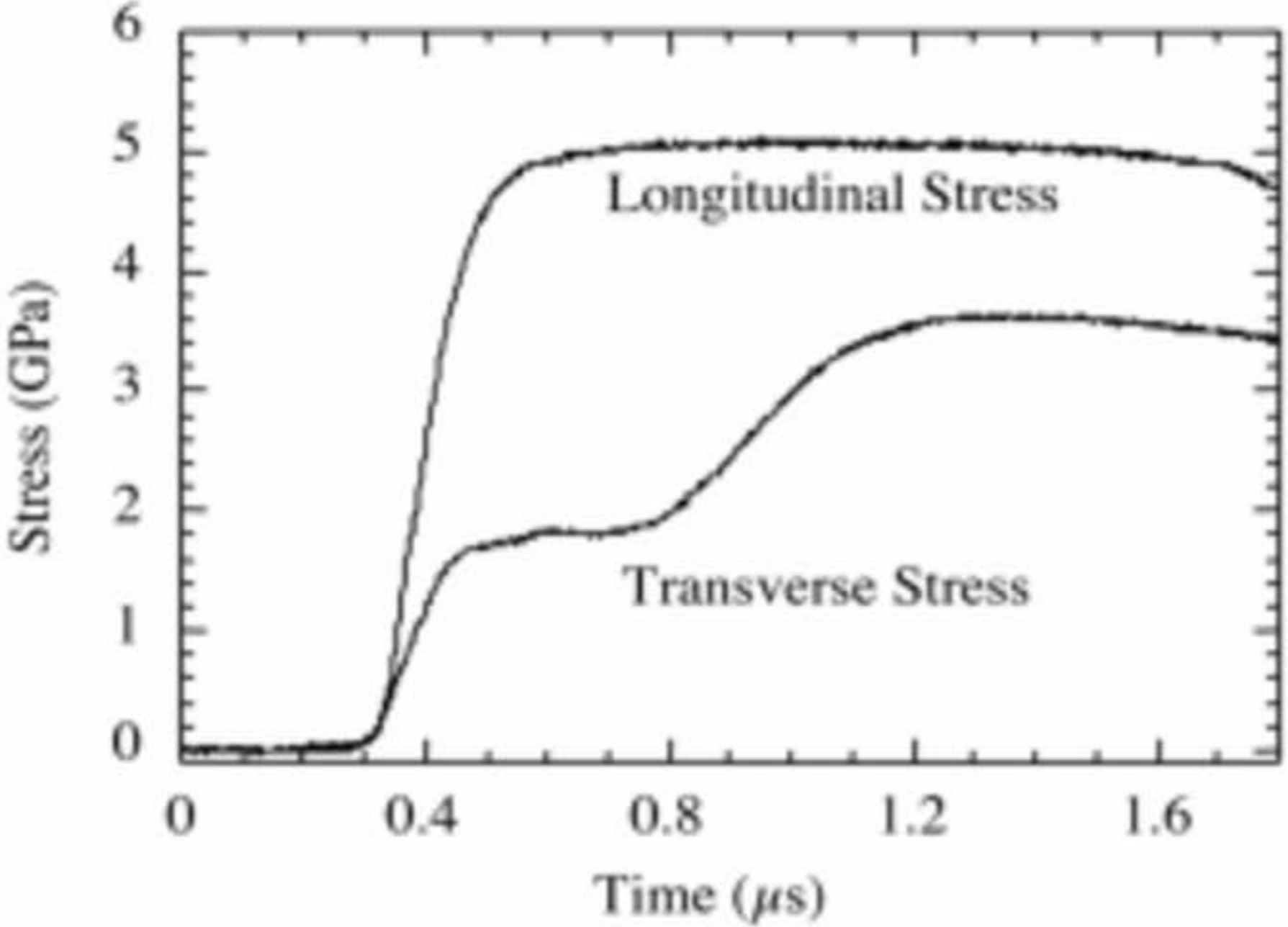
Stress (GPa)
6
5
4
3
2
1
0
Longitudinal Stress
Transverse Stress
0
0.4
0.8
1.2
1.6
Time (μs)

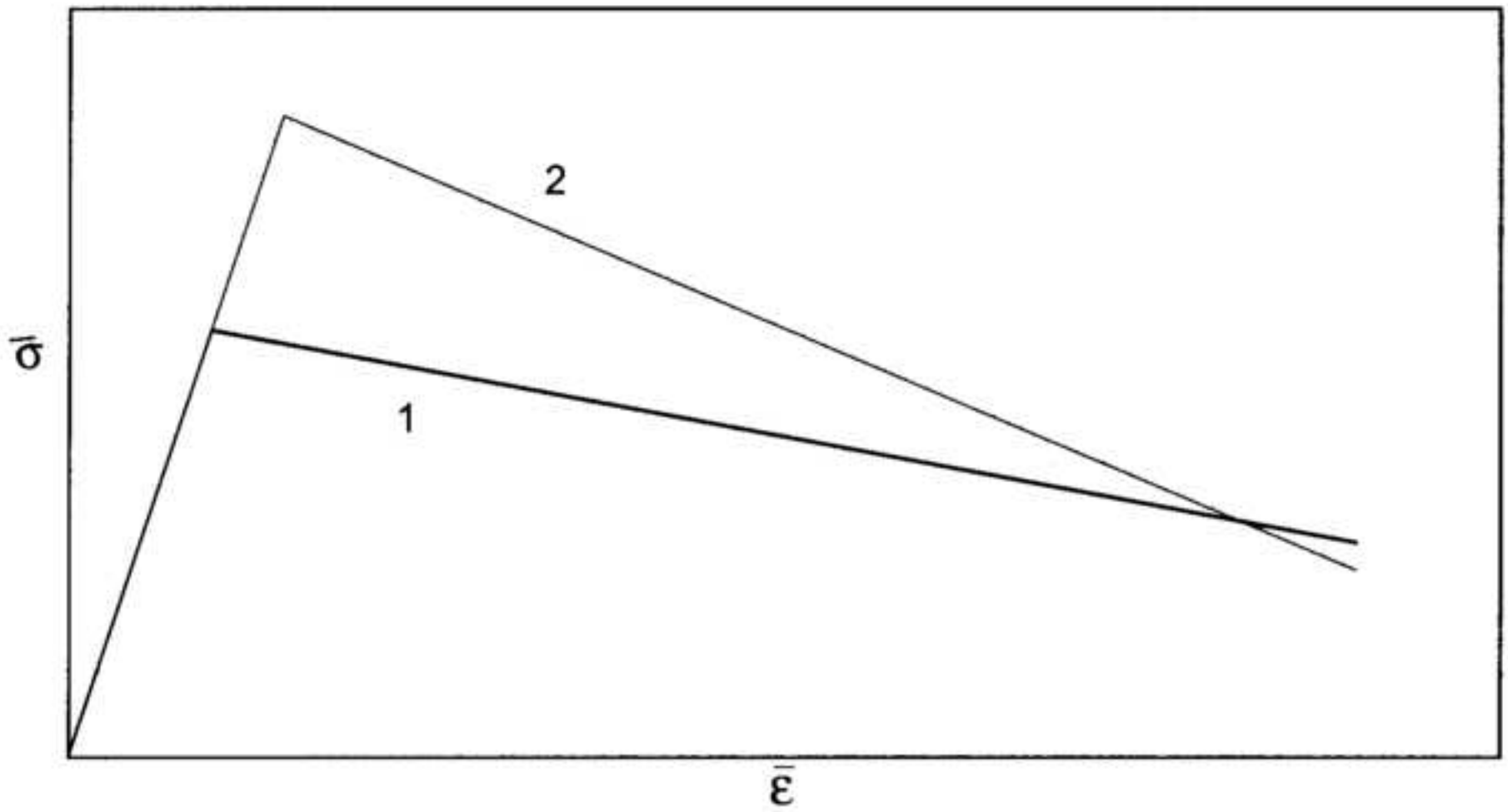
2
1
$\bar{\sigma}$
$\bar{\varepsilon}$

Table 1a.

Relevant properties of the EN3B mild steel used.

Density/kg m^{-3}	**Longitudinal sound speed/mm μs^{-1}**	**Quasistatic yield stress/MPa**	**Dynamic yield stress (@3,500 s^{-1})/MPa**	**Diameter/mm**
7818	5.9	440	940	9.5

Table 1b.

Relevant properties of the borosilicate glass specimens used.

Density/kg m^{-3}	**Longitudinal sound speed/mm μs^{-1}**	**Shear wave speed c_s/mm μs^{-1}**	**Dimensions for high-speed photography/mm**	**Dimensions for X-ray flash studies/mm**
2490	6.05	3.69	75x75x25	60x30x20

Table 2*a*

Parameters of the glass model used (see equation 3)

A/MPa	800
B/MPa	80
m	0.3
C/MPa	-8000

Table 2*b*

Mie-Grüneisen parameters for the borosilicate glass

Density/kg m^{-3}	2490
Bulk sound speed / m s^{-1}	4564
Hugoniot slope coefficient S (=dUs/dU_p)	1.73
Grüneisen gamma	0.53